Edge-Pumped Quasi-Three-Level Slab Lasers: Design and Power Scaling

Todd S. Rutherford, William M. Tulloch, Eric K. Gustafson, and Robert L. Byer, *Fellow, IEEE*

***Abstract*—We present a novel design for a quasi-three-level laser. The design uses a slab laser configuration with the pump light incident from the slab edge. This allows a lower threshold and better power scaling than a conventional face-pumped slab. We present an analytic description of pumping optimization, thermal distortion, and power scaling. Several point designs illustrating power scaling are also described.**

***Index Terms*—Laser thermal factors, modeling, optical distortion, optical pumping, power lasers.**

I. Introduction

SOLID-STATE lasers with high average powers are useful in a wide variety of applications. These include materials processing [1]–[4], remote sensing [5], free space communications [6], laser particle acceleration [7], and gravitational wave interferometry [8]. All of these applications benefit from lasers that are compact, efficient, robust, and have good beam quality. Quasi-three-level lasers generally offer improvements in these areas compared to four-level lasers due to a higher photon efficiency and the associated lower thermal loading. Quasi-three-level lasers have been demonstrated in a variety of configurations. At low powers, microchip [9], [10] designs, waveguides [11], [12], and nonplanar ring layouts [13] have been used. In medium average power ranges with lower peak powers, fiber lasers [14], [15] provide an efficient and compact solution. At high peak and average powers, rod lasers, both end-pumped [16] and side-pumped [17], [18] as well as thin disk geometries [19], [20] have been demonstrated. However, all of these designs have limits on the power that can be extracted from a single gain element with good beam quality.

The zigzag slab geometry has traditionally been used to scale solid-state lasers to high peak and average powers. See, for instance, [21]–[24] and references contained therein. However, conventional slab designs have been difficult to apply to quasi-three-level lasers because of the high pump brightness required to overcome the thermal population of the lower laser level.

We present a novel zigzag slab design which uses pumping along the slab's edge to effectively increase the pumping brightness. Modeling of the pump absorption, thermal performance, and power scaling of this design are presented.

Manuscript received July 6, 1999; revised October 14, 1999. This work was supported in part by the National Science Foundation under Grant PHY-9722119, by the Air Force Office of Scientific Research under Grant F49620-99-1-0270, by the National Aeronautics and Space Administration under NASA Grant NAG5-7709, and by a Grant from the TRW Foundation.

The authors are with the Edward L. Ginzton Laboratory of Physics, Stanford University, Stanford, CA 94305 USA.

Publisher Item Identifier S 0018-9197(00)00960-X.

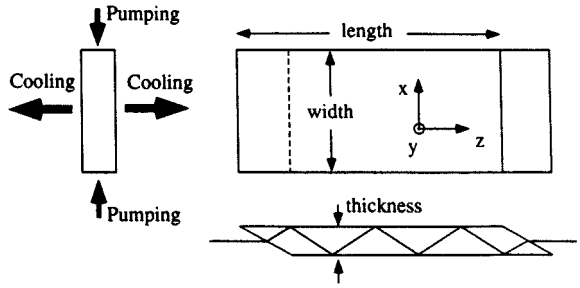

Fig. 1. Orthographic drawing of an edge-pumped zigzag slab.

II. Edge-Pumping Geometry

The edge-pumping geometry is shown in Fig. 1. The cooling and the zigzag path are the same as in a conventional zigzag slab laser design, which we refer to as face-pumping [25]. In both geometries, the cooling is through the large slab faces and the laser mode follows a zigzag path between these faces by multiple total internal reflections (TIR's). As a result, the effect of the primary thermal gradient in the laser medium due to the cooling is averaged by the zigzag path of the laser mode [26].

In the edge-pumped slab, the pump light is incident normal to both the plane of cooling and the plane of laser beam propagation. The pump absorption is thus in the direction of the larger cross-sectional dimension, unlike a face-pumped slab which has pump light entering through the large TIR faces, along the smallest slab dimension.

The edge-pumped design realizes the separation of the pumping and cooling interfaces. The first benefit of this separation is the simplification of the laser head engineering, as discussed in the next section. This advantage applies to four-level as well as quasi-three-level lasers. Our Nd : YAG edge-pumped zigzag slab laser has demonstrated 127 W of multimode output power from 300 W of pump power (see [27] for earlier results). The second advantage applies mostly to quasi-three-level media, where pumping along the slab width allows a longer absorption path and hence lower doping. This means a significant reduction of the quasi-three-level laser threshold.

We define a coordinate system with respect to the slab as follows. The x direction is along the width, y is along the thickness, and z is along the length. The full width is w, the full thickness is t, and the full length is L. The origin is taken as the center of mass of the slab, so $-w/2 < x < w/2$, $-t/2 < y < t/2$, and $-L/2 < z < L/2$.

III. Engineering Advantages

The engineering advantages of edge-pumping are derived from the separation of the pumping and cooling interfaces. The performance of each interface can be individually optimized. Face-pumped slabs typically require a cooling fluid which is transparent to the pump light and directly impinges on the slab. In an edge-pumped slab, heat can be removed by direct conduction to an opaque heat sink. Thus, the contamination associated with the direct flow of cooling fluid over optical surfaces is eliminated. Because the heat sink can be cooled by a separate fluid loop, the cleanliness and optical properties of the cooling fluid are unimportant. Also, mechanical stability is improved by removing the turbulent fluid flow from direct contact with the slab. The heat sink can be tailored to optimize the temperature distribution within the laser gain medium, which reduces residual distortions.

Pumping through the slab edges improves the optical efficiency of the laser. The pump light can be directly coupled to the slab with no intermediate optics or materials. Total internal reflection guides the pump light along the width. For example, a YAG crystal ($n = 1.82$) with an SiO_2 coating ($n = 1.45$) on the TIR faces captures pump light at all incident angles. This pump light trapping due to TIR increases the effective brightness and is crucial for quasi-three-level lasers. The edge faces require only a basic polish and antireflection coating for essentially lossless transmission. The result is an optomechanical design that is simple, robust, and efficient. The Nd : YAG edge-pumped slab mentioned above has demonstrated 42% overall optical efficiency.

IV. Pumping Uniformity

The main challenge for the edge-pumped slab geometry is to achieve uniform pump absorption along the width, since optical distortions of the crystal in this direction are not compensated by the zigzag path. For unsaturated absorption of the pump light, achieving perfectly uniform pump absorption is not possible. The slab edges near the pump source are always pumped harder than the slab center. However, as we show in this section, in practical cases this deviation can be made quite small. In subsequent sections, we compare the size of optical distortions created by the nonuniform pumping with those caused by stress effects that are present in any finite slab [28].

The analysis of the pumping begins with a calculation of the pump absorption profile along the slab width. We treat only the case of symmetric pumping from both slab edges. Single-sided or uneven double-sided pumping can be examined with a simple extension of the following methods. For simplicity, we consider the pump light to be a uniform plane wave. In reality, the pump may have some divergence and intensity nonuniformities, but the main results of this section still apply. The divergence of the pump beam can be included in the analysis by defining an effective absorption coefficient which is larger than the true one, to account for the slightly increased optical path. Also, intensity variations of the pump beam in the yz plane are averaged to first order by the zigzag optical path.

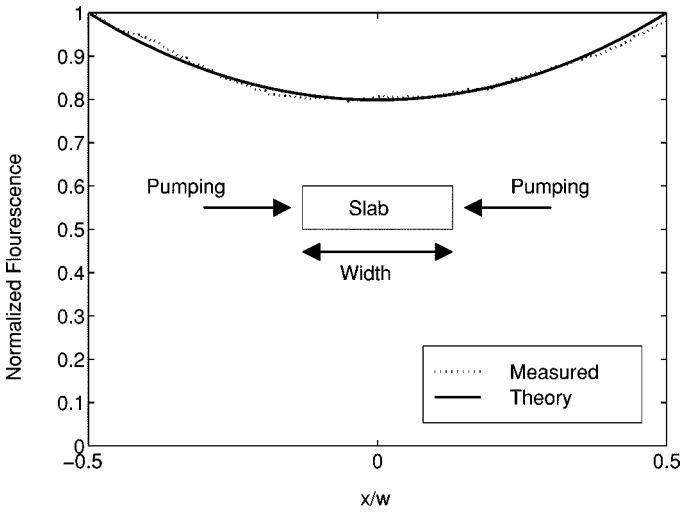

Fig. 2. The measured and calculated normalized fluorescence in an edge-pumped slab versus the normalized slab width. The slab width is 4.5 mm and the theory line uses $\alpha = 3.1$ cm^{-1}. Since the plot is normalized, R_p does affect the fit.

In cases of practical interest, all of the pump light is not absorbed in a single pass through the slab. We define a pump reflectivity R_p as the fraction of the pump light exiting the slab at $x = \pm w/2$ that is reflected back into the slab. For simplicity, R_p is taken as the average pump reflectivity over the entire edge face. In reality, there are some areas on the edge that are highly reflective and other areas where the pump light enters which need to be highly transmitting. With the above assumptions and allowing for an infinite number of pump light passes with reflectivity R_p between each pass, the absorbed pump power density as a function of the position x along the slab width is given by

$$\rho_{\text{abs}}(x) = \frac{\alpha P_p}{tL} \frac{\exp\left(-\frac{\alpha w}{2}\right)}{1 - R_p e^{-\alpha w}} \cosh(\alpha x) \tag{1}$$

where

P_p	total pump power incident on the slab;
$\alpha = n_d \sigma_a$	pump absorption coefficient;
n_d	dopant concentration;
σ_a	effective absorption cross section.

The validity of (1) is shown by comparison with experiment in Fig. 2. The pump absorption data were acquired by imaging the fluorescence at 1064 nm from a Nd : YAG edge-pumped slab. The slab was pumped by fiber-coupled laser diodes with a 600-μm diameter, 0.4 NA fibers. Stray pump light was removed with a filter. The figure shows the fluorescence, which is proportional to the absorbed power, as a function of position along the 4.5-mm-wide slab. Also shown is a fit to (1) with $\alpha = 3.1$ cm^{-1}, which is in good agreement with the expected value for the absorption of laser diode light in 1% doped Nd : YAG. This example illustrates that the shape of the pump distribution depends on α only, while the magnitude depends on α, w, R_p, and P_p/tL.

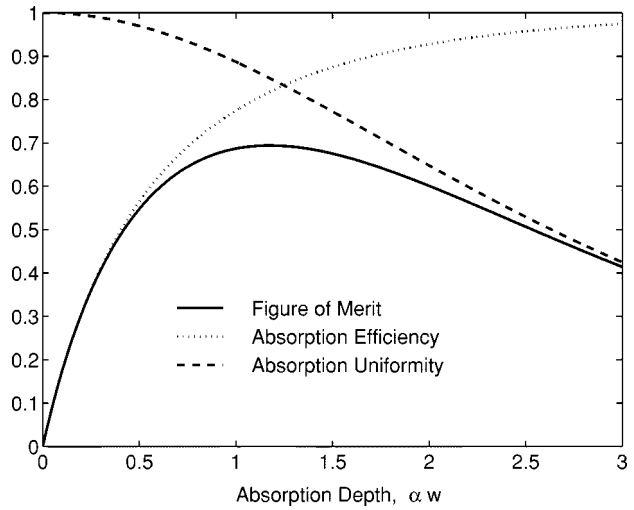

Fig. 3. The pump absorption efficiency, pump absorption uniformity, and pumping figure of merit as a function of the absorption depth αw. In this case, with $R_p = 0.5$, the ideal doping length product is about 1.2.

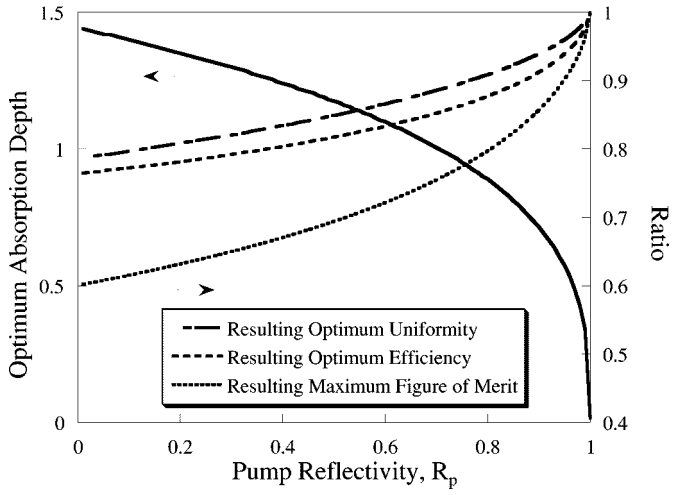

Fig. 4. The optimum αw product as a function of the pump reflectivity R_p. Also shown are the pump absorption efficiency, uniformity, and pumping figure of merit which can be achieved at this optimum condition.

Using (1), we can quantify the pumping performance. The pumping efficiency is simply the total absorbed pump power divided by the total incident pump power

$$\eta_{\rm abs} = \frac{tL\displaystyle\int_{-(w/2)}^{(w/2)} \rho_{\rm abs}(x)\,dx}{P_p} = \frac{1-e^{-\alpha w}}{1-R_p e^{-\alpha w}}. \qquad (2)$$

Therefore, $\eta_{\rm abs}$ depends only on the dimensionless variables R_p and αw. The variable αw, which we call the absorption depth, is proportional to the product of the doping and the width. As expected, $\eta_{\rm abs}$ goes to 1 as R_p goes to 1, regardless of the absorption coefficient. In practice, however, R_p is limited by the need to have some nonreflective areas through which to inject the pump beam, but, as shown in Fig. 4, efficient operation is still possible with lower values of R_p.

Next, we define the pumping uniformity as the pump power absorbed per unit area at the point of least absorption compared to that at the point of greatest absorption. In this case, those points are the center and edge of the slab, respectively. Using (1), we find

$$U = \frac{\rho_{\rm abs}(0)}{\rho_{\rm abs}\left(\frac{w}{2}\right)} = \operatorname{sech}\left(\frac{\alpha w}{2}\right). \qquad (3)$$

Interestingly, the pumping uniformity does not depend upon R_p. However, larger reflectivity can lead to better uniformity because αw can be reduced while maintaining the efficiency. This can be better understood by defining a pumping figure of merit. Since larger absorption depths lead to good efficiency but low uniformity and small absorption depths have the opposite effect, a natural pumping figure of merit is the product of the pump efficiency with the pump absorption uniformity $F_{\rm pump} = U\eta_{\rm abs}$ which can be written as

$$F_{\rm pump} = \frac{1-e^{-\alpha w}}{1-R_p e^{-\alpha w}} \operatorname{sech}\left(\frac{\alpha w}{2}\right). \qquad (4)$$

Fig. 3 shows a plot of the efficiency, uniformity, and pumping figure of merit as a function of absorption depth for $R_p = 0.5$. We see that there is an optimum value for the absorption depth which maximizes the pumping figure of merit. This optimum is useful for choosing the slab width and doping level in a practical design. Fig. 4 shows this optimum αw as a function of R_p, along with the optimum pump absorption efficiency, uniformity, and figure of merit that result. We see that, for lower R_p, the ideal absorption depth is larger and the maximum figure of merit is smaller. Conversely, as R_p approaches 1, the doping can be reduced toward zero, while the efficiency and uniformity rise toward 1. However, even at values of the reflectivity considerably less than 1, a reasonable figure of merit is still possible.

The results derived in this section are valid in the case where there is no saturation of the pump absorption. This assumption is usually reasonable in oscillators since the upper manifold population is clamped at the threshold value regardless of the pumping strength. As an example, consider Yb : YAG at room temperature, where 5.6% of the total number of dopant atoms must be pumped into the upper $^2F_{5/2}$ manifold to equate the upper and lower laser level populations. This transparency point is thus reached without significant reduction in the ground state population. Laser operation clamps the upper manifold population close to this point, so pump bleaching can be ignored. However, the no-saturation assumption may be violated if the medium is operating at high temperatures, where significant thermal depopulation of the ground state occurs. We treat this regime in the model for the laser oscillator output power presented in Section IX.

Operation of an edge-pumped slab in an energy storage mode with low pulse repetition frequency (PRF) results in several changes to the design described above. First, saturation of the pump absorption is a significant effect in this regime. Second, suppression of parasitic oscillations may dictate a lower value of R_p or the use of a pump reflector that has higher loss at the laser wavelength. For the remainder of this paper, we consider only edge-pumped slab lasers operating in a CW or high PRF pulse format.

V. Temperature Effects

Knowledge of the slab temperature distribution is required before we can proceed with an analysis of the laser performance. This is because the population of the lower laser level increases with increasing temperature. Also, temperature gradients along the width give rise to optical distortions which are not cancelled by the zigzag path. We follow the notation used in [26] and write the slab temperature in terms of an average temperature T_a and a position-dependent term which averages to zero over the slab cross section $T'(x, y)$ so that

$$T(x, y) = T_a + T'(x, y). \tag{5}$$

Here and in the rest of the paper, we assume uniform temperature along the slab length, creating a two-dimensional (2-D) solution in the xy plane. The pump light is assumed to be a uniform plane wave incident from both slab edges, as in Section IV. The edges of the slab are insulated, which is a good approximation in a slab that is actively cooled through the large TIR faces.

Calculation of the temperature and stress in the slab is greatly simplified by using a 2-D approximation. This means that the end effects are ignored. However, end effects are largely unaffected by the change to edge-pumping and there is empirical evidence that these effects can be greatly reduced by leaving an unpumped region of the slab of length greater than w at each end [21], [29], [30]. In a quasi-three-level laser, these unpumped regions can be realized by bonding undoped material to each end of the slab, eliminating reabsorption losses from the unpumped regions [16]. A detailed calculation of the 2-D temperature distribution is provided in Appendix B; the important results are summarized in this section.

A. Average Temperature

The average temperature of the slab is determined by the thermal conductance of the slab itself, λ_{slab}, and the thermal conductance between the slab and the coolant, λ_{head}. Starting with (B17),

$$T_a = T_c + \frac{Q_0 t}{2\lambda_{\text{head}}} + \frac{Q_0 t^2}{12k} \tag{6}$$

where

- T_c coolant temperature;
- k thermal conductivity of the slab;
- Q_0 average slab heating per unit volume.

By comparing the last two terms, an effective thermal conductance of the slab can be defined as $\lambda_{\text{slab}} = 6k/t$. Table I shows the thermal conductivities of some common hosts and laser head components. Using the result (B15) for Q_0 and writing the overall thermal resistance $1/\lambda_c = 1/\lambda_{\text{head}} + 1/\lambda_{\text{slab}}$, we can restate (6) as

$$T_a = T_c + \frac{\eta_h \overline{\rho}_{\text{abs}} t}{2\lambda_c} \tag{7}$$

where η_h is the heat fraction and $\overline{\rho}_{\text{abs}}$ is the absorbed pump power per unit volume given in (1), averaged over the slab width.

TABLE I
Comparison of the Thermal Conductance of Various Materials and Configurations

Material	Thickness (mm)	λ_c(W/cm^{2}K)
YAG slab (λ_{slab})	1.5	4
Copper	5	8
Aluminum	5	4.7
SiO_2	.01	13.8
Indium	0.5	16.4
Silicon	1	14.9

The effect of the increase in temperature on the performance of the laser can be calculated as follows. First we define some standard terms for quasi-three-level lasers, following [32]–[35]. The dopant atom density is n_d. The density of atoms in the upper manifold is n_U, and the density of atoms in the ground state manifold is n_L. By conservation of atoms

$$n_d = n_U + n_L. \tag{8}$$

The fraction of the atoms in the ground state manifold which are in the lower laser level is f_a and the fraction of the atoms in the upper manifold which are in the upper laser level is f_b. f_a and f_b are computed from a Boltzmann distribution (A1) and (A2) and are thus functions of the average slab temperature. The gain medium becomes transparent at the lasing wavelength when

$$f_b n_U = f_a n_L. \tag{9}$$

Using (8) and (9) to eliminate n_L gives the density of atoms in the upper manifold at the transparency point

$$n_U = n_d \frac{f_a}{f_a + f_b}. \tag{10}$$

Since each absorbed pump photon moves one atom from the ground state manifold to the upper manifold for an average of one upper manifold lifetime τ, the steady-state absorbed pump power per unit volume can be written as

$$\overline{\rho}_{\text{abs}} = n_U \frac{h\nu_p}{\tau} \tag{11}$$

where h is Planck's constant and ν_p is the frequency of the pump light. Transparency at the laser wavelength is reached when the upper and lower laser level populations are equal. Combining (10) and (11) gives the result for the absorbed pump power density at the transparency point, $\overline{\rho}_{\text{trans}}$,

$$\overline{\rho}_{\text{trans}} = \frac{h\nu_p n_d}{\tau} \frac{f_a(T_a)}{f_a(T_a) + f_b(T_a)} \tag{12}$$

which is the result given in [32]. Since f_a and f_b depend on the crystal temperature and the average temperature depends on pump power by (7), finding $\overline{\rho}_{\text{trans}}$ involves the simultaneous solution of (7) and (12). Fig. 5 shows the example of Yb : YAG with two different doping levels. The important thing to notice is that, below a critical thermal conductance λ_{crit}, the transparency point increases sharply.

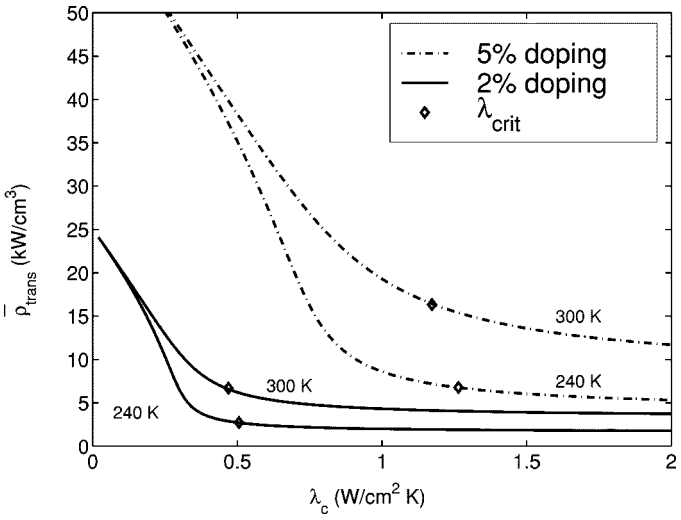

Fig. 5. The absorbed pump power density required to reach transparency in Yb : YAG as a function of the overall thermal conductance for several doping levels and coolant temperatures. Also shown on each curve is the critical thermal conductance $\lambda_{\rm crit}$, calculated using (13). The slab thickness is 1.5 mm and the pump wavelength is 940 nm.

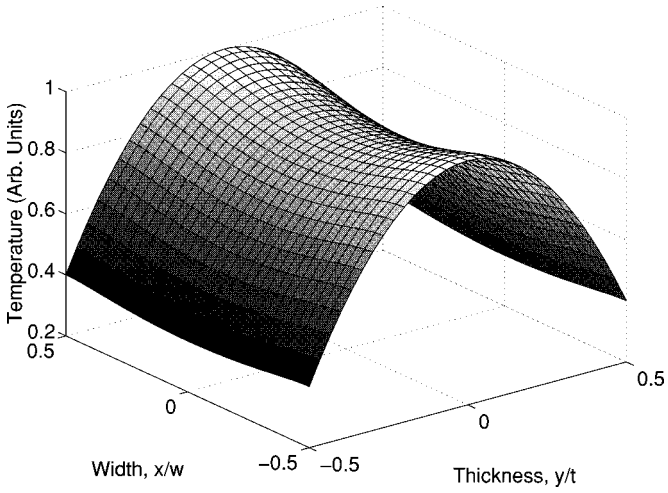

Fig. 6. The normalized temperature distribution of an edge-pumped slab referenced to the coolant temperature ($T = 0$). The pumping is along the width and the cooling is through the faces at $y/t = \pm 0.5$. The aspect ratio is 6, $\alpha w = 1$, and $\lambda_{\rm head}/\lambda_{\rm slab} = 1$. Because the thermal conductance of the heat sink is finite, the temperature at the side of the slab is not equal to the coolant temperature.

We can write this critical conductance $\lambda_{\rm crit}$ as a function of the doping, the thickness, and the coolant temperature. The calculation is presented in Appendix A. The result (A7) is

$$\lambda_{\rm crit} = \left(\frac{h\nu_p\eta_h k_B}{2\Delta E_{\rm eff}\tau}\right)\left(\frac{m_u}{m_u+m_L} - \frac{f_a(T_c)}{f_a(T_c)+f_b(T_c)}\right) t n_d \tag{13}$$

where

k_B Boltzmann's constant;

m_u number of Stark levels in the upper manifold;

m_L number of Stark levels in the lower manifold;

$\Delta E_{\rm eff}$ effective energy splitting defined in (A6).

For example, in Yb : YAG, $m_u = 3$, $m_L = 4$, and $\Delta E_{\rm eff} = 241$ cm^{-1}.

Using (13), we can begin to see the advantages of the edge-pumping concept. The only parameters in (13) that are free once the dopant and host materials are chosen are T_c, t, and n_d. Since it is desirable for $\lambda_{\rm crit}$ to be as small as possible, we want to reduce t and n_d. However, in a face-pumped slab, the product of t and n_d must remain fixed to maintain efficient pump absorption. Thus, for a face-pumped zigzag slab, the only remaining option for reducing $\overline{\rho}_{\rm trans}$ is to lower the coolant temperature, but using a coolant below a few degrees Celsius is undesirable from a practical point of view. Edge-pumping solves this dilemma since t can be made small without sacrificing pump absorption. This is shown in detail in Section VIII. Also, the doping density can be reduced by increasing the slab width to maintain the same absorption depth. Thus, an edge-pumped slab has lower critical thermal conductance than a face-pumped design.

B. Temperature Gradients

In this section, the temperature gradients in the slab are computed using the absorbed pump power density (1). The resulting temperature distribution for the normalized position along the slab width x/w and the normalized position along the slab thickness y/t is derived in Appendix B as (B18). We can write the temperature as a function of the absorption depth αw, the slab aspect ratio $a_r = w/t$, the ratio of the thermal conductance of the heat sink to that of the slab $\lambda_{\rm head}/\lambda_{\rm slab}$, and the pump power per unit length P_p/L as

$$\begin{aligned} T'(x,y) = \frac{2\eta_h\eta_{\rm abs}P_p/L}{a_r k}\Bigg\{ & \frac{1}{16}\left[\frac{1}{3} - \left(\frac{2y}{t}\right)^2\right] \\ & + \sum_{n=1}^{\infty} \frac{(-1)^n a_r^2}{4n^2\pi^2}\frac{(\alpha w)^2}{(\alpha w)^2 + 4n^2\pi^2} \\ & \times \left(1 - \frac{\dfrac{\lambda_{\rm head}}{\lambda_{\rm slab}}\cosh\left(\dfrac{2n\pi}{a_r}\right)\dfrac{y}{t}}{\dfrac{n\pi}{3a_r}\sinh\left(\dfrac{n\pi}{a_r}\right) + \dfrac{\lambda_{\rm head}}{\lambda_{\rm slab}}\cosh\left(\dfrac{n\pi}{a_r}\right)}\right) \\ & \times \cos\left(2n\pi\frac{x}{w}\right)\Bigg\}. \end{aligned} \tag{14}$$

Fig. 6 shows the shape of $T'(x, y)$ for a slab with an aspect ratio of 6. The distribution has a saddle shape, with the hottest regions at the center of each edge face. The effect of the zigzag path in the slab is to average the temperature in the y direction. So, to first order, only the temperature gradients in the x direction lead to optical distortions through changes of index of refraction and thermal expansion. We can analyze these distortions by integrating (14) over y, leaving only the dependence on the width. Define

$$\overline{T}'(x) = \frac{1}{t}\int_{-(t/2)}^{(t/2)} T'(x,y)\,dy \tag{15}$$

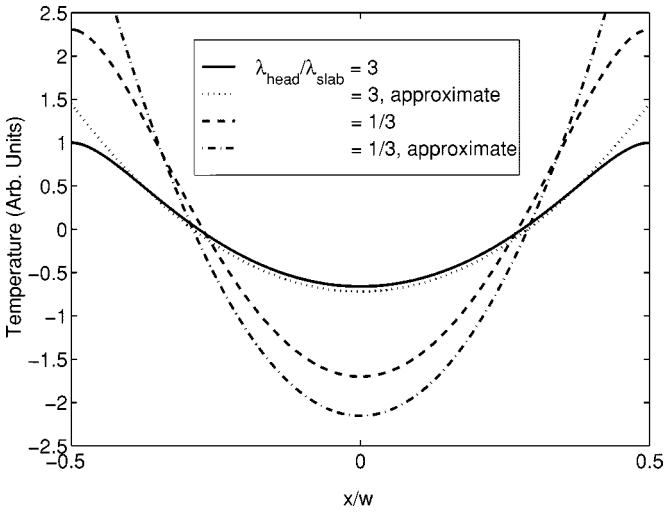

Fig. 7. The normalized temperature averaged over the slab thickness as a function of the position along the slab width for several different thermal conductance values. Here the aspect ratio is 6 and $\alpha w = 1$.

which, using (14), yields the result

$$\overline{T}'(x) = \frac{2\eta_h\eta_{\rm abs}P_p/L}{k} \times \sum_{n=1}^{\infty} \frac{(-1)^n a_r}{4n^2\pi^2} \frac{(\alpha w)^2}{(\alpha w)^2 + 4n^2\pi^2} \times \left(1 - \frac{\frac{\lambda_{\rm head}}{\lambda_{\rm slab}}\frac{a_r}{n\pi}}{\frac{n\pi}{3a_r} + \frac{\lambda_{\rm head}}{\lambda_{\rm slab}}\coth\left(\frac{n\pi}{a_r}\right)}\right) \cos\left(2n\pi\frac{x}{w}\right). \tag{16}$$

We can further simplify (16) if we assume that $w \gg t$. Then the temperature over the center of the slab, more than one thickness away from the edge faces at $x = \pm w/2$, is derived in Appendix B as

$$\overline{T}'_{\rm mid}(x) = \frac{\eta_h\eta_{\rm abs}P_p/L}{k}\frac{1}{12a_r}\left(1 + \frac{\lambda_{\rm slab}}{\lambda_{\rm head}}\right) \times \left(\frac{\alpha w}{2}\frac{\cosh(\alpha x)}{\sinh\left(\frac{\alpha w}{2}\right)} - 1\right). \tag{17}$$

Fig. 7 shows the exact (16) and approximate (17) normalized temperatures along the slab width. As expected, the approximate expression shows a good agreement in the center of the slab, but does not have the correct behavior near the slab edges. The temperature distribution is plotted for several different values of the heat sink thermal conductance. We see that a lower heat sink conductance increases the size of the center to edge thermal gradient in addition to increasing the average temperature of the slab (7). Also, the approximate solution is less accurate as $\lambda_{\rm slab} \gg \lambda_{\rm head}$.

VI. Stress Effects

Heating within the slab gives rise to stress in the laser host material. This thermal stress causes optical distortions, and at higher power levels, catastrophic failure due to fracture. Solution of the full three dimensional problem is best left to numerical solution for the specific slab shape under consideration. In this section we look for a closed form approximation in the two dimensional plane strain limit that provides some insight and can be used in scaling arguments presented later.

The derivation is presented in Appendix C. Equations (C12) and (C13) give approximate expressions for the stress components σ_{xx} and σ_{yy} that are valid more than one thickness away from each slab edge. For calculating optical distortions due to thermal stresses, we are interested in the y-averaged stresses

$$\overline{\sigma}_{xx} = \frac{1}{t}\int_{-t/2}^{t/2} \sigma_{xx}\, dy = 0 \tag{18}$$

$$\overline{\sigma}_{yy} = \frac{1}{t}\int_{-t/2}^{t/2} \sigma_{yy}\, dy = \frac{\eta_h\eta_{\rm abs}P_p/L}{M_s}\frac{(\alpha w)^3}{a_r^3\sinh\left(\frac{\alpha w}{2}\right)}\frac{\cosh(\alpha x)}{1440} \tag{19}$$

where $M_s = (1-\nu)k/\alpha_t E$, ν is Poisson's ratio, α_t is the thermal expansion coefficient, and E is the modulus of elasticity. The only stress component of concern for optical distortions is thus $\overline{\sigma}_{yy}$, which varies along the width as $\cosh(\alpha x)$. Next we compute the total optical path length change due to nonuniform temperature and stress in an edge-pumped slab.

VII. Optical Distortion

Optical path length variations across the width of the slab are due to several different effects. In this section, we follow the approach outlined in [28, Section III-C] to analyze these distortions. In general, these effects may be separated into those proportional to temperature and those proportional to stress by writing the width-dependent path length change Δp as

$$\Delta p(x) = (dn/dT_{\rm slab})l_{\rm eff}\overline{T}'(x) - B_{\rm slab}l_{\rm eff}\overline{\sigma}_{yy}(x) \tag{20}$$

where $l_{\rm eff} = L/\sin\theta$ is the geometric length of the zigzag path. The values of $dn/dT_{\rm slab}$ and $B_{\rm slab}$ depend on the polarization and the TIR bounce angle θ, as well as material parameters [28].

Using (17) and (19) in (20) gives the approximate path length change across the central part of the slab width. Since both $\overline{T}'_{\rm mid}$ and $\overline{\sigma}_{yy}$ have the same $\cosh(\alpha x)$ dependence, we can find the lowest order distortion by expanding $\cosh$ in a power series. Ignoring the constant terms, the resulting path length change is

$$\Delta p(x) = \frac{\eta_h\eta_{\rm abs}\alpha w P_p/L}{2a_r\sinh\left(\frac{\alpha w}{2}\right)}l_{\rm eff}(\alpha x)^2 \times \left(\frac{dn}{dT}_{\rm slab}\frac{1+\frac{\lambda_{\rm slab}}{\lambda_{\rm head}}}{24k} - B_{\rm slab}\frac{(\alpha w)^2}{1440M_s a_r^2}\right) \tag{21}$$

and, for small distortions, (21) can be written in terms of a thin lens with focal power given by

$$\frac{1}{F} = -\frac{\eta_h \eta_{\rm abs} (\alpha w)^3 P_p / L}{w^2 a_r \sinh\left(\frac{\alpha w}{2}\right)} l_{\rm eff} \times \left(\frac{dn}{dT}_{\rm slab} \frac{1 + \frac{\lambda_{\rm slab}}{\lambda_{\rm head}}}{24k} - B_{\rm slab} \frac{(\alpha w)^2}{1440 M_s a_r^2} \right) \quad (22)$$

where F is the lens focal length. For a Brewster-end YAG slab with p-polarized light, $a_r = 6$, $\alpha w = 1$, and $\lambda_{\rm slab} = \lambda_{\rm head}$, the lensing is dominated by dn/dT and the focal length is

$$F(\text{meters}) = -37 \left(\frac{\eta_h \eta_{\rm abs} P_p}{100\,\text{W}} \right)^{-1} \left(\frac{w}{1\,\text{cm}} \right)^2. \quad (23)$$

So we see that the focusing caused by edge-pumping is weak. In practice, the lensing in these crystals is dominated by end effects that are present regardless of the pumping direction.

Thus far we have ignored the heat sink which is in contact with the slab. In fact, this heat sink offers another method for controlling the residual distortions due to nonuniform absorption. An appropriate variation of the thermal resistance $\lambda_{\rm head}$ of the heat sink along the width has the effect of altering the boundary conditions used to solve (B1). An in-depth examination of this solution is beyond the scope of this paper. In the simplest realization, this effect could be achieved in a metal heat sink by using multiple coolant channels at varying distances from the slab.

VIII. Power Scaling

The promise of the zigzag slab geometry is the potential to scale the laser to high powers without significant optical distortion or thermal fracture. In this section, we compare the quasi-three-level power scaling of the edge-pumped slab with that of other laser geometries. Yb : YAG pumped at 940 nm is taken as an example.

Consider a laser medium which is uniformly pumped in some volume V. For any configuration, the absorbed pump power required to reach transparency P_T is found from (12) by multiplying by the pumped volume

$$P_T = \frac{h\nu_p n_d V}{\tau} \frac{f_a}{f_a + f_b}. \quad (24)$$

It is important to note that this transparency pump power depends directly on the total number of dopant atoms.

One limit on the absorbed pump power is the stress fracture of the laser medium [26]. The absorbed pump power at the point of stress fracture P_F depends upon material parameters and the shape of the laser medium. Each configuration is treated separately in the following sections.

We require that $P_T < P_F$ for the laser to reach threshold prior to fracture. The thermal problems discussed in Section V get worse as the slab gets closer to stress fracture, so the ability to operate well below stress fracture and well above transparency is desirable. The ratio $\Gamma = P_F / P_T$ thus provides a good figure of merit for the robustness of the laser design. A larger Γ is desired since the laser can be operated farther above transparency. Next we find Γ for a face-pumped slab, an edge-pumped slab, a side-pumped rod, and a thin disk.

A. Face-Pumped Slab

For a uniformly pumped and cooled slab, the absorbed pump power at the stress fracture limit [26] is given by

$$P_F = \frac{12 R_s}{\eta_h} \left(\frac{w}{t} \right) L \quad (25)$$

where $R_s = M_s \sigma_{\max}$ and $\sigma_{\max}$ is the tensile stress at fracture, which depends upon the mechanical properties and surface preparation of the laser material. Using (24) and (25) gives Γ for a slab

$$\Gamma_{\rm slab} = \left(\frac{12 R_s \tau}{\eta_h h \nu_p} \right) \left(\frac{f_a + f_b}{f_a} \right) \frac{1}{n_d t^2}. \quad (26)$$

The first term contains material parameters and the second contains the temperature dependence of the upper and lower laser level populations. The third term contains all of the geometrical information.

Equation (2) gave the absorption efficiency for an edge-pumped slab. A similar expression gives the absorption efficiency for a face-pumped slab

$$\eta_{\rm abs} = \frac{1 - e^{-\alpha t}}{1 - R_p e^{-\alpha t}}. \quad (27)$$

If we assume that $\eta_{\rm abs}$ must be above some minimum acceptable value $\eta_{\min}$ to have a practical design, then solving (27) for t gives the constraint

$$t \geq \frac{1}{\sigma_a n_d^{\max}} \ln \left(\frac{1 - R_p \eta_{\min}}{1 - \eta_{\min}} \right) \quad (28)$$

where $n_d^{\max}$ is the maximum dopant concentration for the crystal. For some laser media that can be highly doped (Yb : YAG), the thickness limit at lower pump powers may be due to fabrication or laser mode size constraints. However, we ignore this case since we are considering power scaling.

The stress fracture concerns require t to be small, (26), and pump absorption efficiency considerations require t to be large, (28). Combining (26) and (27) gives Γ for a face-pumped slab, with the added constraint that t must satisfy (28):

$$\Gamma_{\rm face} = \left(\frac{12 R_s \tau \sigma_a}{\eta_h h \nu_p} \right) \left(\frac{f_a + f_b}{f_a} \right) \frac{1}{\ln \left(\frac{1 - R_p \eta_{\min}}{1 - \eta_{\min}} \right)} \frac{1}{t}. \quad (29)$$

The only parameters available to the laser designer are t (although it is still constrained by (28), since n_d cannot be made arbitrarily large) and R_p, which is fundamentally limited by the need to couple the pump light uniformly into the large TIR face.

B. Edge-Pumped Slab

By moving to edge-pumping, we eliminate the tradeoff between pump absorption and stress fracture. Equation (2) gives the absorption efficiency for an edge-pumped slab. Solving (2) gives

$$n_d \geq \frac{1}{\sigma_a w} \ln\left(\frac{1-R_p\eta_{\min}}{1-\eta_{\min}}\right) \tag{30}$$

and substituting into (26) gives the ratio for edge-pumping

$$\Gamma_{\text{edge}} = \left(\frac{12R_s\tau\sigma_a}{\eta_h h\nu_p}\right)\left(\frac{f_a+f_b}{f_a}\right)\frac{1}{\ln\left(\frac{1-R_p\eta_{\min}}{1-\eta_{\min}}\right)}\frac{w}{t^2}. \tag{31}$$

Now t is subject only to fabrication constraints, so, to increase Γ_{edge}, t can be reduced, and independently w can be increased to reach an acceptable pump absorption efficiency.

C. Side-Pumped Rod

For a rod geometry laser, the absorbed power at the stress fracture limit is [26]

$$P_F = \frac{8\pi R_s}{\eta_h} L \tag{32}$$

where L is the rod length. Using (24) and (32) gives

$$\Gamma_{\text{rod}} = \left(\frac{12R_s\tau}{\eta_h h\nu_p}\right)\left(\frac{f_a+f_b}{f_a}\right)\frac{8}{3n_d d^2}. \tag{33}$$

where d is the rod diameter.

Next we define the pump absorption efficiency for the rod

$$\eta_{\text{abs}} = \frac{1-e^{-\alpha d}}{1-R_p e^{-\alpha d}} \tag{34}$$

where R_p is the reflectivity after each pump light pass through the rod. This result is optimistic since many pump rays do not travel through the full diameter.

Solving (34) for d gives the constraint

$$d \geq \frac{1}{\sigma_a n_d^{\max}} \ln\left(\frac{1-R_p\eta_{\min}}{1-\eta_{\min}}\right) \tag{35}$$

which is substituted into (33) to give

$$\Gamma_{\text{rod}} = \left(\frac{12R_s\tau\sigma_a}{\eta_h h\nu_p}\right)\left(\frac{f_a+f_b}{f_a}\right)\frac{1}{\ln\left(\frac{1-R_p\eta_{\min}}{1-\eta_{\min}}\right)}\frac{8}{3d} \tag{36}$$

where d is constrained by (35) so that the only way to increase Γ_{rod} is to increase R_p. This is the approach taken in [18]. However, as was the case for the face-pumped slab, R_p cannot be increased arbitrarily since openings must be left for the pump light to enter.

D. Thin Disk

For a thin disk [19] of thickness t, the absorbed pump power at the stress fracture limit is

$$P_F = \frac{12R_s}{\eta_h}\left(\frac{A}{t}\right) \tag{37}$$

assuming uniform pumping of a spot with area A where the pump spot diameter is larger than t. Combining (24) and (37) gives

$$\Gamma_{\text{disk}} = \left(\frac{12R_s\tau}{\eta_h h\nu_p}\right)\left(\frac{f_a+f_b}{f_a}\right)\frac{1}{n_d t^2} \tag{38}$$

which is the same as (26), as expected. The pump absorption efficiency for the thin disk is

$$\eta_{\text{abs}} = 1 - e^{-N\alpha t} \tag{39}$$

where N is the number of passes of the pump light through the crystal. Solving (39) for t gives the constraint

$$t \geq \frac{1}{\sigma_a n_d^{\max} N} \ln\left(\frac{1}{1-\eta_{\min}}\right) \tag{40}$$

and substituting into (38) yields

$$\Gamma_{\text{disk}} = \left(\frac{12R_s\tau\sigma_a}{\eta_h h\nu_p}\right)\left(\frac{f_a+f_b}{f_a}\right)\frac{1}{\ln\left(\frac{1}{1-\eta_{\min}}\right)}\frac{N}{t}. \tag{41}$$

Improvement of the thin disk geometry is accomplished by decreasing t subject to the limit imposed by (40) and increasing the number of pump light passes N.

E. Configuration Comparison

Now we can compare the figure of merit for each of the geometries. Comparing the power scaling figure of merit for the two slab geometries gives the simple result

$$\frac{\Gamma_{\text{edge}}}{\Gamma_{\text{face}}} = \frac{w}{t}. \tag{42}$$

Therefore, the edge-pumped design is better by a factor equal to the aspect ratio of the slab, which is always greater than one.

Comparing the edge-pumped slab to a side-pumped rod, we find

$$\frac{\Gamma_{\text{edge}}}{\Gamma_{\text{rod}}} = \frac{3}{8}\frac{w}{t}\frac{d}{t}. \tag{43}$$

For a gain medium with comparable minor dimensions ($d \sim t$), the edge-pumped slab has a higher figure of merit as long as the aspect ratio is greater than 8/3.

Making the comparison of the edge-pumped slab to a thin disk gives

$$\frac{\Gamma_{\text{edge}}}{\Gamma_{\text{disk}}} = \frac{\ln\left(\frac{1}{1-\eta_{\min}}\right)}{\ln\left(\frac{1-R_p\eta_{\min}}{1-\eta_{\min}}\right)}\frac{a_r}{N}. \tag{44}$$

TABLE II
A COMPARISON OF THE VALUE OF THE FIGURE OF MERIT $\Gamma = P_F/P_T$ FOR THE FOUR CONFIGURATIONS DISCUSSED IN THE TEXT*. LARGER Γ INDICATES THE POTENTIAL FOR OPERATION FARTHER ABOVE TRANSPARENCY

$\Gamma = P_F/P_T$	Temperature (K)		
	240	300	400
Edge-pumped Slab	113.7	55.6	28.7
Face-pumped Slab	11.4	5.6	2.9
Side-pumped Rod	30.3	14.8	7.7
Thin Disk	168	81.9	42.3

*The assumptions here are 15% pump reflectivity R_p, 80% pump absorption $\eta_{\min}$, a slab aspect ratio of 10, slab thickness $t = 1$ mm, rod diameter $d = 1$ mm, and 16 pump light passes N through the thin disk.

So, in the worst case where $R_p = 0$, the slab is better if the aspect ratio is larger than the number of thin disk pump light passes N. Currently the highest reported number of passes is 16 [20].

Table II shows the figure of merit Γ for Yb : YAG pumped at 940 nm. As expected, the figure of merit improves as the temperature is decreased. Also, the edge-pumped slab and thin disk configurations have higher Γ than the side-pumped rod or face-pumped slab.

IX. LASER OSCILLATOR MODEL

We now present a model for the output power of an edge-pumped quasi-three-level slab laser. The approach used below is based on the theory of [33], altered to treat the case of an edge-pumped slab. The model includes the effect of depletion of the lower manifold, arbitrarily large gain and output coupling, and the self-heating described by (7).

First we treat the case of multiple transverse mode oscillation, where the laser mode completely fills the slab. The overall excitation rate of atoms from the lower manifold to the upper manifold is then

$$\Re_{\text{ex}} = \eta_{\text{abs}} \frac{P_p}{h\nu_p} \tag{45}$$

and the overall de-excitation rate can be written by tracing the mode around the cavity to track the stimulated emission and then adding a spontaneous emission term

$$\begin{aligned}\Re_{\text{de-ex}} = \frac{P_{\text{out}}}{h\nu_L} \frac{\mathcal{R}_{\text{oc}}}{1-\mathcal{R}_{\text{oc}}} \left[(e^{\beta\sigma\Delta n l_{\text{eff}}} - 1) \right. \\ \left. + (1-\delta)^2 (e^{2\beta\sigma\Delta n l_{\text{eff}}} - e^{\beta\sigma\Delta n l_{\text{eff}}}) \right] \\ + \frac{n_U w t L}{\tau}\end{aligned} \tag{46}$$

where

- ν_L laser frequency;
- $\mathcal{R}_{\text{oc}}$ output coupler reflectivity;
- Δn population inversion density on the laser transition;
- δ one-way cavity loss;
- P_{out} laser output power.

β is a zigzag overlap factor which measures the amount of beam overlap in the zigzag path. β varies from 1 when there is no overlap at the bounce points (an infinitely small beam) to 2 when there is complete overlap (a beam which totally fills the slab). At steady state, the rate of excitation must match that of de-excitation, so we equate (45) and (46) and solve for the output power

$$\begin{aligned}P_{\text{out}} = \frac{\nu_L}{\nu_p} \frac{1-\mathcal{R}_{\text{oc}}}{\mathcal{R}_{\text{oc}}((1-\delta)^2 e^{\beta\sigma\Delta n l_{\text{eff}}} + 1)(e^{\beta\sigma\Delta n l_{\text{eff}}} - 1)} \\ \times \left(\eta_{\text{abs}} P_p - \frac{h\nu_p}{\tau} w t L n_U \right).\end{aligned} \tag{47}$$

Next we find the value for the upper manifold population n_U. This is done by setting the round-trip gain of the resonator equal to one, $\mathcal{R}_{\text{oc}}(1-\delta)^2 e^{2\beta\sigma\Delta n l_{\text{eff}}} = 1$, solving for Δn and using the identity $\Delta n = f_b n_U - f_a n_L$. The result is

$$n_U = \frac{1}{2f\beta\sigma l_{\text{eff}}} \ln \left[\frac{1}{\mathcal{R}_{\text{oc}}(1-\delta)^2} \right] + \frac{f_a}{f} n_d \tag{48}$$

where $f = f_a + f_b$. The only other term in (47) that needs to be found is η_{abs}. We generalize (2) to include depopulation of the lower pump level by writing $\alpha = \sigma_a (f_a' n_L - f_b' n_U)$, where f_a' is the fraction of the lower manifold atoms which are in the lower pump level and f_b' is the fraction of upper manifold atoms which are in the upper pump level. Using this relation for α, (48), and the conservation of atoms gives the result

$$\eta_{\text{abs}} = \frac{1 - e^{-\sigma_a \Delta n_{\text{eff}} w}}{1 - R_p e^{-\sigma_a \Delta n_{\text{eff}} w}} \tag{49}$$

where Δn_{eff} is given by

$$\Delta n_{\text{eff}} = \frac{f_a' f - f_a f'}{f} n_d - \frac{f'}{f} \frac{1}{2\beta\sigma l_{\text{eff}}} \ln \left[\frac{1}{\mathcal{R}_{\text{oc}}(1-\delta)^2} \right]. \tag{50}$$

On their face, (47)–(50) provide an explicit solution for the output power. However, all the Boltzmann population fractions depend upon the absorbed pump power $\eta_{\text{abs}} P_p$ due to the self-heating of the slab. Thus, (49) is really an implicit equation which requires a numerical solution. We can avoid this difficulty by assuming that the self-heating is proportional to the incident pump power P_p. This means that the heating will be somewhat overestimated when the pump absorption is decreased by saturation from its unsaturated pumping value. As a result, we underestimate the output power at high pump powers. So long as the pump absorption has not been drastically reduced, the approximation is a good one.

To model a TEM_{00} mode laser, we simply include a mode overlap term η_{mode} in the overall efficiency. The final result is

$$\begin{aligned}P_{\text{out}} = \eta_{\text{mode}} \frac{\nu_L}{\nu_p} \frac{1-\mathcal{R}_{\text{oc}}}{1-\mathcal{R}_{\text{oc}} + \sqrt{\mathcal{R}_{\text{oc}}} \left(\frac{1}{1-\delta} + \delta - 1 \right)} \\ \times \left(\eta_{\text{abs}} P_p - \frac{h\nu_p w t L}{2f\beta\sigma\tau l_{\text{eff}}} \ln \left[\frac{1}{\mathcal{R}_{\text{oc}}(1-\delta)^2} \right] \right. \\ \left. - \frac{h\nu_p}{\tau} \frac{f_a}{f} n_d w t L \right).\end{aligned} \tag{51}$$

A. Practical Limits

In addition to (51), the design of edge-pumped slab lasers has some practical constraints. We have already mentioned heat removal, thermal- and stress-induced distortions, and pumping

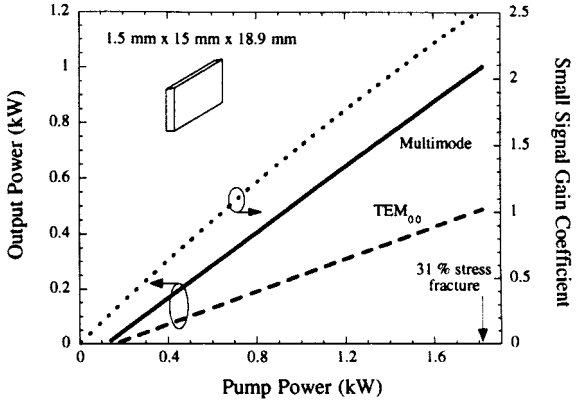

Fig. 8. The predicted laser oscillator performance for a 1-kW edge-pumped Nd : YAG slab laser.

uniformity. In addition, the area of the edge faces must be large enough to accommodate the available pump light.

Parasitic oscillations and gain saturation by amplified spontaneous emission (ASE) also place a limit on the small-signal gain in TEM_{00} oscillators. In low-repetition-rate pulsed lasers with energy storage, the small-signal gain coefficient must be kept below about $g_0 l_{\text{eff}} = 2.5$ [36], [37] to prevent significant energy loss by this mechanism. The effect is not as severe in CW oscillators, so, for the point designs that follow, we take $g_0 l_{\text{eff}} < 3.5$ as a conservative limit.

As the width of the slab is increased beyond a few millimeters, laser extraction in a fundamental mode which fills the entire width becomes difficult due to the large mode size required. However, TEM_{00} output is still possible in these large aspect ratio slabs. Folded resonator configurations that pass a smaller beam through the slab at several positions can extract power from a large fraction of the slab volume. In the next section, we assume that resonator extraction can be modeled with the single-mode overlap term η_{mode}. More detailed calculations of extraction from end-pumped quasi-three-level lasers are presented in [34] and [38].

B. Point Designs

Using (51), we develop point designs at several power levels in Nd : YAG and Yb : YAG. Also included is a calculation of the small-signal gain, which requires a numerical solution for Δn. All the point designs meet the optimum pumping condition at full pump power, as well as all the other constraints mentioned above.

We take as a starting point the edge-pumped Nd : YAG slab laser we have demonstrated, which generated 127 W of multimode output power with 300 W of incident pump power. Extending this result one order of magnitude, we arrive at a point design for a 1 kW Nd : YAG laser, shown in Fig. 8. All the point designs assume $\eta_{\text{mode}} = 1$ and $\beta = 2$ for a multimode oscillator and $\eta_{\text{mode}} = 0.5$ and $\beta = 1.5$ for a TEM_{00} oscillator. The other parameters used in this design are shown in Table III, along with the measured parameters from the demonstrated 127-W edge-pumped slab. The calculated parameters in Table III are found using the results derived earlier, with the exception of R_p, which is found by a comparison of the pumping area to the total area of the edges

$$R_p = \frac{P_{\max}/I_{\text{pump}}}{2tL} \tag{52}$$

where $P_{\max}$ is the maximum pump power required for the point design and I_{pump} is the available pump brightness. The values assumed for I_{pump} correspond to commercially available laser diodes (50 W from a 440-μm-diameter fiber gives $I_{\text{pump}} = 32.9$ kW/cm^2).

From Fig. 8, we see that the small-signal gain of the Nd : YAG laser is approaching $e^{2.5}$ at 2 kW of pump power. Power scaling of Nd : YAG is thus limited by the parasitic and ASE problems mentioned above. However, with a smaller stimulated emission cross section, Yb : YAG does not reach this gain limit until much higher powers.

To illustrate the power scaling that is possible with the edge-pumped design, we present three point designs for an edge-pumped Yb : YAG slab. The parameters for these point designs are also shown in Table III. Figs. 9–11 show the results for 1-, 10-, and 100-kW point designs in Yb : YAG pumped at 940 nm. Results for 968-nm pumping are similar, since the slightly increased photon efficiency is offset by the lower absorption cross section. By increasing the aspect ratio and decreasing the doping, the edge-pumped slab can be scaled to high powers. Notice that the lasers stay at roughly the same proportion of stress fracture, and the pump power density decreases as we move to higher powers. Because of the lower pump power densities, the average temperature increase in the 100-kW slab is lower than in the 1-kW slab.

X. Conclusions

The edge-pumped zigzag slab laser geometry offers a robust, scalable laser design. By using separate crystal surfaces for pumping, cooling, and laser extraction, each boundary can be individually optimized. A small pumping gradient along the slab width results from exponential absorption of the pump light. However, we have shown that, with proper choice of the absorption depth αw, the optical distortions due to the pumping gradient are smaller than the distortions present in any zigzag slab due to end effects.

For quasi-three-level lasers, an edge-pumped slab laser can have a low threshold. The long path length along the width for large aspect ratio slabs means that the doping can be reduced without compromising pump absorption efficiency. This translates to reduced threshold which is critical for quasi-three-level lasers. The edge-pumped slab is thus power scalable by increasing the aspect ratio, which improves the cooling and reduces the doping. Comparison with existing quasi-three-level laser geometries shows that the edge-pumped slab is capable of operation much farther above threshold than either a face-pumped slab or a side-pumped rod and is comparable to a thin disk design. Moreover, it can operate at higher average powers.

Oscillator modeling of Yb : YAG edge-pumped slab lasers including depletion of the lower laser manifold was performed.

TABLE III
DESIGN PARAMETERS FOR EDGE-PUMPED Nd : YAG AND Yb : YAG LASERS. ALSO SHOWN ARE THE MEASURED PARAMETERS OF A DEMONSTRATED 127-W EDGE-PUMPED Nd : YAG LASER

		Nd:YAG		Yb:YAG		
		Experiment	Theory	Theory		
Parameter	Units	127 W	1 kW	1 kW	10 kW	100 kW
Design Inputs						
Thickness	cm	0.15	0.15	0.08	0.12	0.27
Width	cm	0.45	1.5	0.48	1.80	8.18
Length	cm	3.84	1.89	1.0	3.03	12.89
Coolant temperature, T_c	K	283	300	300	300	300
Laser head thermal conductance, λ_{head}	W/cm^{2}K	2.1	2	2	2	2
Single-pass loss, δ	%	1.5	1.3	1.3	2.1	3.5
Pump brightness	kW/cm^2	3.5	19.7	32.9	32.9	32.9
Calculated Results						
Average temperature rise, $T_a - T_c$	K	29	66	108	95	62
Thermal lens focal power (width)	m^{-1}	-2.4	-0.11	-0.79	-0.22	-0.03
Pump reflectivity, R_p	%	60	77	57	14	11
Dopant concentration	% at.	1.0	0.26	2.4	0.8	0.17
Pumping density, P_p/wtL	kW/cm^3	1.8	4.3	47	27	6.0
Overall optical efficiency	%	42.3	56	55	57	58

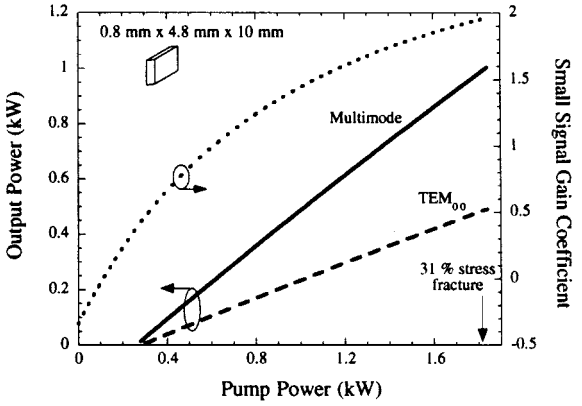

Fig. 9. The predicted laser oscillator performance for a 1-kW edge-pumped Yb : YAG slab laser.

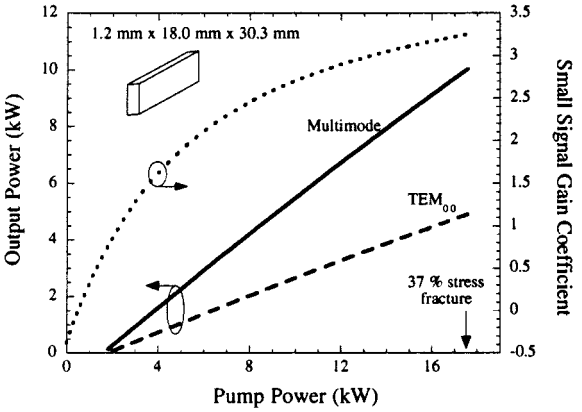

Fig. 10. The predicted laser oscillator performance for a 10-kW edge-pumped Yb : YAG slab laser.

Point designs with comparable heat removal, pump power densities, and overall efficiency at the 1-, 10-, and 100-kW output power levels illustrate the scaling of the edge-pumped slab design. The most powerful aspect of edge-pumping a quasi-three-level slab laser is the scaling that is possible by increasing the slab aspect ratio and reducing the doping concentration.

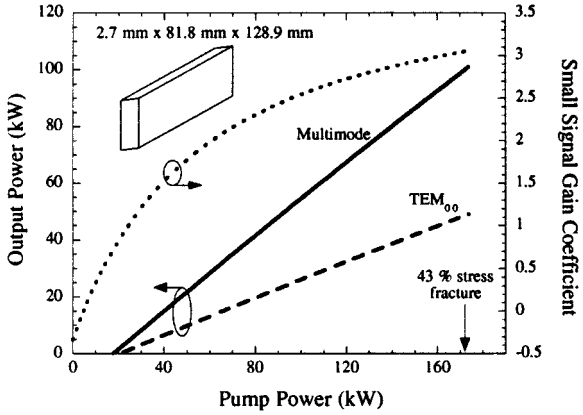

Fig. 11. The predicted laser oscillator performance for a 100-kW edge-pumped Yb : YAG slab laser.

APPENDIX A
CALCULATION OF THE CRITICAL THERMAL CONDUCTANCE

We treat the general case of an energy level structure with an upper and lower manifold, with Stark splitting in each manifold. Call m_L the number of Stark split levels in the lower or ground state manifold and m_u the number in the upper manifold. Then define ΔE_i^L as the energy difference between the ground state and the ith Stark level in the lower manifold. Similarly, ΔE_i^u is the energy split between the lowest level in the upper manifold and the ith level in the upper manifold. The lower and upper laser levels are singled out as ΔE_a and ΔE_b, respectively. The Boltzmann population fractions f_a and f_b for the lower and upper laser levels, respectively, are written as

$$f_a = \frac{e^{-\Delta E_a/k_B T_a}}{\sum_{i=1}^{m_L} e^{-\Delta E_i^L/k_B T_a}} \tag{A1}$$

$$f_b = \frac{e^{-\Delta E_b/k_B T_a}}{\sum_{i=1}^{m_u} e^{-\Delta E_i^u/k_B T_a}}. \tag{A2}$$

In the limit that the thermal conductance λ_c is very large, the average temperature of the slab remains fixed at the coolant temperature and does not increase with absorbed pump power. In this limit, we can write (12) as

$$\overline{\rho}_{\text{trans}} = \frac{h\nu_p n_d}{\tau} \frac{f_a(T_c)}{f_a(T_c) + f_b(T_c)} \tag{A3}$$

which is independent of λ_c.

In the limit that λ_c is small, T_a increases rapidly with pump power, and we can ignore T_c and write

$$T_a = \frac{\eta_h \overline{\rho}_{\text{abs}} t}{2\lambda_c}. \tag{A4}$$

We then proceed to expand (12) to first order in $1/T_a$, which becomes arbitrarily small as λ_c goes to zero. After some algebra, we arrive at

$$\overline{\rho}_{\text{trans}} = \frac{h\nu_p n_d}{\tau} \frac{m_u}{m_u + m_L} - \frac{2\lambda_c \Delta E_{\text{eff}}}{k_B \eta_h t} \tag{A5}$$

which is linearly decreasing with λ_c. Here ΔE_{eff} is an effective energy splitting that can be written as

$$\Delta E_{\text{eff}} = \frac{m_L}{m_u + m_L}(\Delta E_a - \Delta E_b) - \frac{1}{m_u + m_L} \times \sum_{i=1}^{m_L} \Delta E_i^L + \frac{m_L/m_u}{m_u + m_L} \sum_{i=1}^{m_u} \Delta E_i^u. \tag{A6}$$

The critical conductance is found at the point where (A3) and (A5) intersect. Setting these two equations equal and solving for λ_c gives

$$\lambda_{\text{crit}} = \left(\frac{h\nu_p \eta_h k_B}{2\Delta E_{\text{eff}} \tau}\right)\left(\frac{m_u}{m_u + m_L} - \frac{f_a(T_c)}{f_a(T_c) + f_b(T_c)}\right) t n_d \tag{A7}$$

which is written as (13) in the body of the paper.

Appendix B

Calculation of Slab Temperature Distribution

In this appendix, we derive the expression for the 2-D temperature distribution in the slab cross section. We start with the steady-state partial differential equation for conductive heat transfer in an isotropic solid

$$\nabla^2 T(x, y) = -\frac{Q(x)}{k} \tag{B1}$$

where $Q(x)$ is the heat generated per unit volume in the slab and is assumed to be only a function of x, as discussed in Section IV. To keep the equation analytically tractable, we ignore any temperature dependence of the thermal conductivity k. Numerical solutions for a uniformly pumped YAG slab with k a function of temperature can be found in [39]. We assume that the edge faces are insulated so that the first two boundary conditions are

$$\frac{\partial T}{\partial x} = 0, \quad \text{for} \quad x = \pm\frac{w}{2}. \tag{B2}$$

For the second pair of boundary conditions, we use Newton's law of cooling for the large TIR faces of the slab

$$k\frac{\partial T}{\partial y} + \lambda_{\text{head}} T = 0 \quad \text{for} \quad y = \frac{t}{2} \tag{B3}$$

$$-k\frac{\partial T}{\partial y} + \lambda_{\text{head}} T = 0, \quad \text{for} \quad y = -\frac{t}{2} \tag{B4}$$

where we have set $T_c = 0$. This only has the effect of offsetting the entire solution by T_c, which can simply be added back to the final result. Next we expand the temperature in a Fourier series in x

$$T(x, y) = \frac{a_0(y)}{2} + \sum_{n=1}^{\infty} a_n(y) \cos(\beta_n x) \tag{B5}$$

where $\beta_n = 2n\pi/w$, in order to automatically satisfy the boundary conditions (B2). $Q(x)$ can then be expanded in a similar series

$$Q(x) = \frac{A_0}{2} + \sum_{n=1}^{\infty} A_n \cos(\beta_n x) \tag{B6}$$

where the A_n are computed using

$$A_n = \frac{2}{w} \int_{-w/2}^{w/2} Q(x) \cos(\beta_n x)\, dx. \tag{B7}$$

Substituting (B5) and (B6) into (B1) gives

$$\frac{1}{2}\frac{d^2 a_0(y)}{dy^2} + \sum_{n=1}^{\infty} \frac{d^2 a_n(y)}{dy^2} \cos \beta_n x - \sum_{n=1}^{\infty} a_n(y)\beta_n^2 \cos(\beta_n x) = -\frac{A_0}{2k} - \frac{1}{k}\sum_{n=1}^{\infty} A_n \cos \beta_n x. \tag{B8}$$

Using this equation, we can equate terms of equal order in n independently. For the $n = 0$ terms, we have

$$\frac{d^2 a_0(y)}{dy^2} = -\frac{A_0}{k}. \tag{B9}$$

Solving this equation with the boundary conditions (B3) and (B4) gives

$$a_0(y) = \frac{A_0}{k}\left(\frac{t^2}{8} + \frac{tk}{2\lambda_{\text{head}}} - \frac{y^2}{2}\right). \tag{B10}$$

Similarly, the terms where $n \neq 0$ are found from solving

$$\frac{d^2 a_n(y)}{dy^2} - \beta_n^2 a_n(y) = -\frac{A_n}{k} \tag{B11}$$

with the same boundary conditions (B3) and (B4). The result is

$$a_n(y) = \frac{A_n}{k\beta_n^2}\left(1 - \frac{\lambda_{\text{head}} \cosh(\beta_n y)}{k\beta_n \sinh\left(\beta_n \frac{t}{2}\right) + \lambda_{\text{head}} \cosh\left(\beta_n \frac{t}{2}\right)}\right). \tag{B12}$$

All that remains is to find the Fourier coefficients of the pump absorption distribution A_n. For the heat per unit volume, we can write

$$Q(x) = \eta_h \rho_{\text{abs}}(x) \tag{B13}$$

where $\rho_{\text{abs}}(x)$ is known from (1). Application of (B7) using (B13) gives the result

$$A_n = (-1)^n 2Q_0 \frac{(\alpha w)^2}{(\alpha w)^2 + 4n^2\pi^2} \tag{B14}$$

where Q_0 is the overall heating per unit volume and can be written as

$$Q_0 = \frac{\eta_h \eta_{\text{abs}} P_p}{wtL}. \tag{B15}$$

We now have all the pieces in place to write down the temperature equation. Substituting (B10), (B12), and (B14) into (B5), we get

$$T(x,y)=\frac{Q_0t^2}{8k}\left(1+\frac{4k}{\lambda_{\rm head}t}-\left(\frac{2y}{t}\right)^2\right)+\frac{2Q_0}{k}\sum_{n=1}^{\infty}\frac{(-1)^n}{\beta_n^2}\frac{(\alpha w)^2}{(\alpha w)^2+4n^2\pi^2}\times\left(1-\frac{\cosh(\beta_n y)}{\frac{k\beta_n}{\lambda_{\rm head}}\sinh\left(\beta_n\frac{t}{2}\right)+\cosh\left(\beta_n\frac{t}{2}\right)}\right)\cos(\beta_n x). \tag{B16}$$

A result in the form of (5) needs an expression for the average temperature T_a. This is done by integrating (B16) over the slab cross section. If we choose the x integration first, this is an easy task, since all the $\cos(\beta_n x)$ terms integrate to zero. The end result is

$$T_a = T_c + \frac{Q_0 t}{2\lambda_{\rm head}} + \frac{Q_0 t^2}{12k} \tag{B17}$$

where we have added the coolant temperature to provide an absolute point of reference. By subtracting the second and third terms in (B17) from (B16), we arrive at the second difference temperature term in (5). Along the way, we also express everything in terms of the pump power per unit length P_p/L and the dimensionless variables αw, $a_r = w/t$, $\lambda_{\rm head}/\lambda_{\rm slab}$, x/w, and y/t

$$T'(x,y)=\frac{2\eta_h\eta_{\rm abs}P_p/L}{a_r k}\left\{\frac{1}{16}\left[\frac{1}{3}-\left(\frac{2y}{t}\right)^2\right]+\sum_{n=1}^{\infty}\frac{(-1)^n a_r^2}{4n^2\pi^2}\frac{(\alpha w)^2}{(\alpha w)^2+4n^2\pi^2}\times\left(1-\frac{\frac{\lambda_{\rm head}}{\lambda_{\rm slab}}\cosh\left(\frac{2n\pi}{a_r}\frac{y}{t}\right)}{\frac{n\pi}{3a_r}\sinh\left(\frac{n\pi}{a_r}\right)+\frac{\lambda_{\rm head}}{\lambda_{\rm slab}}\cosh\left(\frac{n\pi}{a_r}\right)}\right)\times\cos\left(2n\pi\frac{x}{w}\right)\right\}. \tag{B18}$$

A simpler expression for $T'(x,y)$ can be found if we ignore the flow of heat in the x direction. This approximation is valid in the central region of the slab, more than one thickness away from each edge, i.e., for the region $-w/2+t < x < w/2-t$. Of course this means that what follows is only valid for slabs with aspect ratios greater than 2. Instead of (B1), we ignore $\partial^2 T/\partial x^2$ and write

$$\frac{\partial^2 T_{\rm mid}}{\partial y^2} = -\frac{Q(x)}{k}. \tag{B19}$$

Using the same Newton's law of cooling boundary conditions written as (B3) and (B5), we find

$$T_{\rm mid}(x,y) = \frac{Q(x)t^2}{2k}\left(\frac{\lambda_{\rm slab}}{6\lambda_{\rm head}}+\frac{1}{4}-\left(\frac{y}{t}\right)^2\right) \tag{B20}$$

and $T'_{\rm mid}(x,y) = T_{\rm mid}(x,y) - T_a$.

For calculation of the thermal lensing across the center of the slab, we need $\overline{T}'_{\rm mid}(x)$, which is found by integrating $T'_{\rm mid}(x,y)$ over the thickness. The result, including the explicit expression (B13) for $Q(x)$, is

$$\overline{T}'_{\rm mid}(x) = \frac{\eta_h\eta_{\rm abs}P_p/L}{k}\frac{1}{12a_r}\left(1+\frac{\lambda_{\rm slab}}{\lambda_{\rm head}}\right)\times\left(\frac{\alpha w}{2}\frac{\cosh(\alpha x)}{\sinh\left(\frac{\alpha w}{2}\right)}-1\right). \tag{B21}$$

APPENDIX C

CALCULATION OF APPROXIMATE SLAB STRESS DISTRIBUTION

Here we are interested in calculating a relatively simple analytic approximation for the stress developed in an edge-pumped slab with pump absorption given by (B13). We begin with two important assumptions. First, we invoke the plane strain approximation [28], [40] to reduce the problem to two dimensions. This is equivalent to assuming that the slab is infinitely long with pumping and cooling independent of z. As the point designs in Section IX-B showed, the width of the slab begins to approach the length in some cases. This means that the conditions for plane strain are not perfectly met. However, the results are still valid for order of magnitude scaling arguments.

The second approximation is to ignore the areas within one slab thickness of the edge of the slab. According to Saint–Venant's principle, the boundaries at $x = \pm w/2$ only influence the stress within about one thickness of the slab edge. Thus the results are valid in the central area of slabs with aspect ratio of at least 2.

In the plane strain limit, the stresses can be found from the Airy stress potential ϕ, which obeys the partial differential equation for a simply connected isotropic medium

$$\nabla^2\,\nabla^2\,\phi = \frac{Q(x)}{M_s} \tag{C1}$$

with boundary conditions

$$\phi = \frac{\partial\phi}{\partial x} = 0 \quad \text{at} \quad x = \pm w/2 \tag{C2}$$

$$\phi = \frac{\partial\phi}{\partial y} = 0 \quad \text{at} \quad y = \pm t/2. \tag{C3}$$

Using (B13), we write

$$Q(x) = Q_0\frac{\alpha w}{2\sinh\left(\frac{\alpha w}{2}\right)}\cosh(\alpha x). \tag{C4}$$

Begin by ignoring the partial derivatives with respect to x in (C1) and also the boundary condition at the slab edges, (C2).

The validity of this approach is addressed below. The resulting equation is

$$\frac{\partial^4\phi}{\partial y^4} = \frac{Q_0}{M_s}\frac{\alpha w}{2\sinh\left(\frac{\alpha w}{2}\right)}\cosh(\alpha x) \tag{C5}$$

which, using boundary condition (C3), has the solution

$$\phi = \frac{Q_0}{M_s}\frac{\alpha w}{2\sinh\left(\frac{\alpha w}{2}\right)}\cosh(\alpha x)\left(\frac{y^4}{24} - \frac{t^2y^2}{48} + \frac{t^4}{384}\right). \tag{C6}$$

Now we check the error by substituting (C6) back into (C1). The three terms on the left-hand side are

$$\frac{\partial^4\phi}{\partial y^4} = \frac{Q(x)}{M_s} \tag{C7}$$

$$2\frac{\partial^4\phi}{\partial x^2\partial y^2} = 2(\alpha t)^2\left(\frac{1}{2}\left(\frac{y}{t}\right)^2 - \frac{1}{24}\right)\frac{Q(x)}{M_s} \tag{C8}$$

$$\frac{\partial^4\phi}{\partial x^4} = (\alpha t)^4\left(\frac{1}{24}\left(\frac{y}{t}\right)^4 - \frac{1}{48}\left(\frac{y}{t}\right)^2 + \frac{1}{384}\right)\frac{Q(x)}{M_s} \tag{C9}$$

and, since αw is of order 1, $\alpha t \sim 1/a_r$. Thus, (C8) is at smaller than (C7) by at least $6a_r^2$ and (C9) is smaller by at least $384a_r^4$. So we see that (C6) is a good approximation to ϕ for reasonable aspect ratios and absorption depths.

Now all that remains is to calculate the stresses. The shear stresses σ_{xy} and σ_{yx} are zero since we have assumed that all the surfaces are free. The two remaining stress components are given by

$$\sigma_{xx} = \frac{\partial^2\phi}{\partial y^2} \tag{C10}$$

$$\sigma_{yy} = \frac{\partial^2\phi}{\partial x^2} \tag{C11}$$

so using (C.6) we arrive at the final result

$$\sigma_{xx} = \frac{\eta_h\eta_{\rm abs}P_p/L}{M_s}\frac{(\alpha w)}{2a_r\sinh\left(\frac{\alpha w}{2}\right)}\cosh(\alpha x) \times\left(\frac{1}{2}\left(\frac{y}{t}\right)^2 - \frac{1}{24}\right) \tag{C12}$$

$$\sigma_{yy} = \frac{\eta_h\eta_{\rm abs}P_p/L}{M_s}\frac{(\alpha w)^3}{2a_r^3\sinh\left(\frac{\alpha w}{2}\right)}\cosh(\alpha x) \times\left(\frac{1}{24}\left(\frac{y}{t}\right)^4 - \frac{1}{48}\left(\frac{y}{t}\right)^2 + \frac{1}{384}\right). \tag{C13}$$

ACKNOWLEDGMENT

The authors would like to thank G. Fanning, J. Unternahrer, and W. Lotshaw for helpful discussions.

REFERENCES

[1] P. B. Corkum, "Femtosecond lasers and their implications for materials processing," *Proc. SPIE*, vol. 3274, pp. 10–17, 1998.
[2] K. Du, J. Biesenbach, D. Ehrlichmann, U. Habich, U. Jarosch, J. Klein, P. Loosen, J. Niehoff, and R. Wester, "Lasers for materials processing: Specifications and trends," *Opt. Quantum Electron.*, vol. 27, pp. 1089–1102, Dec. 1995.
[3] M. D. Perry, B. C. Stuart, P. S. Banks, M. D. Feit, and V. Yanovsky, "Ultrashort-pulse laser machining of dielectric materials," *J. Appl. Phys.*, vol. 85, pp. 6803–6810, May 1999.
[4] S. Nolte, C. Momma, H. Jacobs, A. Tunnermann, B. Chichkov, B. Wellegehausen, and H. Welling, "Ablation of metals by ultrashort laser pulses," *J. Opt. Soc. Amer. B*, vol. 14, pp. 2716–2722, Oct. 1997.
[5] I. Melngailis, W. E. Keicher, C. Freed, S. Marcus, B. E. Edwards, A. Sanchez, T. Y. Fan, and D. L. Spears, "Laser radar component technology," in *Proc. IEEE*, vol. 84, Feb. 1996, pp. 227–267.
[6] J. W. Armstrong, C. Yeh, and K. E. Wilson, "Earth-to-deep-space optical communications system with adaptive tilt and scintillation correction by use of near-earth relay mirrors," *Opt. Lett.*, vol. 23, pp. 1087–1089, July 1998.
[7] Y. C. Huang, T. Plettner, R. L. Byer, R. H. Pantell, R. L. Swent, T. I. Smith, J. E. Spencer, R. H. Siemann, and H. Wiedemann, "The physics experiment for a laser-driven electron accelerator," *Nucl. Instrum. Methods A*, vol. 407, pp. 316–321, 1998.
[8] A. Abramovici, W. Althouse, R. Drever, Y. Gursel, S. Kawamura, F. Raab, D. Shoemaker, L. Sievers, R. Spero, K. Thorne, R. Vogt, R. Weiss, S. Whitcomb, and M. Zucker, "LIGO: The laser interferometer gravitational-wave observatory," *Science*, vol. 256, pp. 325–333, Apr. 1992.
[9] P. Lacovara, H. K. Choi, C. A. Wang, R. L. Aggarwal, and T. Y. Fan, "Room-temperature diode-pumped Yb : YAG laser," *Opt. Lett.*, vol. 16, pp. 1089–1091, July 1991.
[10] T. Y. Fan, S. Klunk, and G. Henein, "Diode-pumped Q-switched Yb : YAG laser," *Opt. Lett.*, vol. 18, pp. 423–425, Mar. 1993.
[11] D. Pelenc, B. Chambaz, I. Chartier, B. Ferr, C. Wyon, D. P. Shepherd, D. C. Hanna, A. C. Large, and A. C. Tropper, "High slope efficiency and low threshold in a diode-pumped epitaxially grown Yb : YAG waveguide laser," *Opt. Commun.*, vol. 115, pp. 491–497, April 1995.
[12] U. Griebner and H. Schönnagel, "Laser operation with nearly diffraction-limited output from a Yb : YAG multimode channel waveguide," *Opt. Lett.*, vol. 24, pp. 750–752, June 1999.
[13] I. Freitag, R. Henking, A. Tunnermann, and H. Welling, "Quasithree-level room-temperature Nd : YAG ring laser with high single-frequency output power at 946 nm," *Opt. Lett.*, vol. 20, pp. 2499–2501, Dec. 1995.
[14] M. H. Muendel, "High-power fiber laser studies at the polaroid corporation," *Proc. SPIE*, vol. 3264, pp. 21–29, 1998.
[15] J. Porta, A. B. Grudinin, Z. J. Chen, J. D. Minelly, and N. J. Traynor, "Evironmentally stable picosecond ytterbium fiber laser with a broad tuning range," *Opt. Lett.*, vol. 23, pp. 615–617, April 1998.
[16] E. C. Honea, R. J. Beach, S. C. Mitchell, and P. V. Avizonis, "183-W, $M^2 = 2.4$ Yb : YAG Q-switched laser," *Opt. Lett.*, vol. 24, pp. 154–156, Feb. 1999.
[17] H. Bruesselbach and D. S. Sumida, "69-W-average-power Yb : YAG laser," *Opt. Lett.*, vol. 21, pp. 480–482, Apr. 1996.
[18] D. S. Sumida, H. Bruesselbach, R. W. Byren, M. Mangir, and R. Reeder, "High-power Yb : YAG rod oscillators and amplifiers," *Proc. SPIE*, vol. 3265, pp. 100–105, 1998.
[19] A. Giesen, H. Hugel, A. Voss, K. Wittig, U. Brauch, and H. Opower, "Scalable concept for diode-pumped high-power solid-state lasers," *Appl. Phys. B*, vol. 58, pp. 365–372, May 1994.
[20] S. Erhard, K. Contag, A. Giesen, I. Johannsen, M. Karszewski, T. Rupp, and C. Stewen, "Novel pump design of Yb : YAG thin disk laser for operation at room temperature with improved efficiency," in *Advanced Solid State Lasers OSA*, 1999, pp. 79–81.
[21] G. F. Albrecht, J. M. Eggleston, and J. J. Ewing, "Design and characterization of a high average power slab YAG laser," *IEEE J. Quantum Electron.*, vol. QE-22, pp. 2099–2106, Nov. 1986.
[22] R. J. Shine, A. J. Alfrey, and R. L. Byer, "40-W cw, TEM_{00}-mode, diode-laser-pumped, Nd : YAG miniature-slab laser," *Opt. Lett.*, vol. 20, pp. 459–461, Mar. 1995.
[23] R. J. St. Pierre, G. W. Holleman, M. Valley, H. Injeyan, J. G. Berg, R. C. Hilyard, M. Mitchell, M. E. Weber, J. Zamel, T. Engler, D. Hall, R. Tinti, and J. Machan, "Active tracker laser (ATLAS)," *IEEE J. Select. Topics Quantum Electron.*, vol. 3, pp. 64–70, Feb. 1997.
[24] R. J. St. Pierre, D. W. Mordaunt, H. Injeyan, J. G. Berg, R. C. Hilyard, M. E. Weber, M. G. Wickham, and G. Harpole, "Diode array pumped kilowatt laser," in *Proc. SPIE*, vol. 3264, 1998, pp. 2–8.

[25] W. S. Martin and J. P. Chernoch, "Multiple internal reflection face pumped laser," U.S. Patent 3 633 126, 1972.
[26] J. M. Eggleston, T. J. Kane, K. Kuhn, J. Unternahrer, and R. L. Byer, "The slab geometry laser—Part I: Theory," *IEEE J. Quantum Electron.*, vol. QE-20, pp. 289–301, Mar. 1984.
[27] T. S. Rutherford, W. M. Tulloch, E. K. Gustafson, and R. L. Byer, "A 100 W, edge-pumped, conduction-cooled Nd : YAG zig-zag slab laser with low thermal distortion," in *Conf. Lasers and Electro-Optics in OSA Tech. Dig.*, May 1999, pp. 31–32.
[28] T. J. Kane, J. M. Eggleston, and R. L. Byer, "The slab geometry laser—Part II: Thermal effects in a finite slab," *IEEE J. Quantum Electron.*, vol. QE-21, pp. 1195–1210, Aug. 1985.
[29] T. J. Kane, R. C. Eckardt, and R. L. Byer, "Reduced thermal focussing and birefringence in zig-zag slab geometry crystalline lasers," *IEEE J. Quantum Electron.*, vol. QE-19, pp. 1351–1354, Sept. 1983.
[30] W. Koechner, *Solid-State Laser Engineering*. Berlin, Germany: Springer, 1996.
[31] T. Y. Fan, "Heat generation in Nd : YAG and Yb : YAG," *IEEE J. Quantum Electron.*, vol. 29, pp. 1457–1459, June 1993.
[32] H. W. Bruesselbach, D. S. Sumida, R. A. Reeder, and R. W. Byren, "Low-heat high-power scaling using InGaAs-diode-pumped Yb : YAG lasers," *IEEE J. Select. Topics Quantum Electron.*, vol. 3, pp. 105–116, Feb. 1997.
[33] R. J. Beach, "CW theory of quasi-three level end-pumped laser oscillators," *Opt. Commun.*, vol. 123, pp. 385–393, Jan. 1996.
[34] W. P. Risk, "Modeling of longitudinally pumped solid-state lasers exhibiting reabsorption losses," *J. Opt. Soc. Amer. B*, vol. 5, pp. 1412–1423, July 1988.
[35] T. Y. Fan and R. L. Byer, "Modeling and cw operation of a quasi-three-level 946 nm Nd : YAG laser," *IEEE J. Quantum Electron.*, vol. QE-23, pp. 605–612, May 1987.
[36] D. C. Brown, D. P. Benfey, W. J. Gehm, D. H. Holmes, and K. K. Lee, "Parasitic oscillations and amplified spontaneous emission in face-pumped total internal reflection lasers," in *Proc. SPIE*, vol. 736, 1987, pp. 74–83.
[37] R. Tommasini and J. E. Balmer, "Amplified spontaneous emission and maximum gain-length product revised for general line shapes," *J. Opt. Soc. Amer. B*, vol. 16, pp. 538–545, Apr. 1999.
[38] T. Taira, W. M. Tulloch, and R. L. Byer, "Modeling of quasi-three-level lasers and operation of CW Yb:YAG lasers," *Appl. Opt.*, vol. 36, pp. 1867–1874, Mar. 1997.
[39] D. C. Brown, "Nonlinear thermal and stress effects and scaling behavior of YAG slab amplifiers," *IEEE J. Quantum Electron.*, vol. 34, pp. 2393–2402, Dec. 1998.
[40] B. A. Boley and J. H. Weiner, *Theory of Thermal Stresses*. New York: Dover, 1997.

Todd S. Rutherford received the B.S. degree in applied physics from Yale University, New Haven, CT, in 1995. He is currently working toward the Ph.D. degree at Stanford University, Stanford, CA.

While at Yale, he worked on modeling of the electromagnetic field distributions of near-field scanning optical probes. His present research interests include development of high-average-power diode-pumped solid-state lasers and amplifiers, especially those utilizing Yb : YAG.

Mr. Rutherford is a member of the Optical Society of America and SPIE.

William M. Tulloch received the B.S. degree in engineering physics from the University of the Pacific, Stockton, CA, in 1992 and the M.S. degree in electrical engineering from Stanford University, Stanford, CA, in 1994. He is currently working toward the Ph.D. degree at Stanford University.

His present research interest is in the area of high-average-power laser-diode-pumped solid state lasers, with an emphasis on slab laser engineering. The primary area of interest is the design and characterization of high coherence laser sources for application to laser interferometer gravitational wave detectors. From 1986 to1993, he was employed at Lawrence Livermore National Laboratory (LLNL), Livermore, CA, where he was involved in laser remote sensing and short-pulse high-energy laser research. He is presently on leave of absence from LLNL to continue studies at Stanford University.

Eric K. Gustafson received the B.S. degree in physics from the California Institute of Technology, Pasadena, in 1974 and the Ph.D. in applied physics from Stanford University, Stanford, CA, in 1983. His thesis topic was the development of coherent anti-Stokes Raman scattering in supersonic expansions as a high-resolution spectroscopy technique and his minor field of study was fluid mechanics.

He has worked on gallium-doped germanium photoconductors for far-infrared astronomy, diode-laser-pumped solid-state lasers and their frequency stabilization, and high-power harmonic frequency conversion of CW diode-laser-pumped solid-state lasers. His current research interests are centered on gravitational wave interferometry and include high-power free space laser amplifiers and amplifier noise, limits to interferometer operation set by laser beam heating of optics, interferometer control, and the development of crystalline materials for interferometer core optics.

Robert L. Byer (M'75–M'83–F'87) is a Professor of Applied Physics at Stanford University, Stanford, CA, where he has conducted research and taught classes in lasers and nonlinear optics since 1969. He has made numerous contributions to laser science and technology including the demonstration of the first tunable visible parametric oscillator, the development of the Q-switched unstable resonator Nd : YAG laser, remote sensing using tunable infrared sources, and precision spectroscopy using coherent anti Stokes Raman scattering. Current research includes the development of advanced nonlinear optical materials and laser-diode-pumped solid-state laser sources for applications to gravitational wave detection and to laser particle acceleration. He has published more than 300 scientific papers and holds 35 patents in the fields of lasers and nonlinear optics.

Prof. Byer is a fellow of the Optical Society of America, the American Physical Society, and the American Association for the Advancement of Science. In 1985, he served as president of the IEEE Lasers and Electro-Optics Society and in 1994 he served as the President of the Optical Society of America. He is a founding member of the California Council on Science and Technology and served as chair from 1995 to 1998. He has served on the Engineering Advisory Board of the National Science Foundation. He was Chair of the Applied Physics Department from 1981 to 1984, Associate Dean of Humanities and Sciences from 1985 to 1987, and served as Vice Provost and Dean of Research at Stanford University, Stanford, CA, from 1987 to 1992. He is currently the Director of the Center for Nonlinear Optical Materials at Stanford and the director of the Hansen Experimental Research Laboratory at Stanford. In 1996, he received the Quantum Electronics Award from the IEEE Lasers and Electro-Optics Society. In 1998, he received the Schawlow Award of the Laser Institute of America and the R. W. Wood prize of the Optical Society of America. He was elected to the National Academy of Engineering in 1987.